



**Nanoconfined Iron (III) Fluoride Cathode in NaDFOB
Electrolyte: Towards High-Performance Sodium-Ion
Batteries**

Journal:	<i>Journal of Materials Chemistry A</i>
Manuscript ID	TA-ART-11-2019-012853.R1
Article Type:	Paper
Date Submitted by the Author:	13-Jan-2020
Complete List of Authors:	Sun, Zifei; Georgia Institute of Technology, Fu, Wenbin; Georgia Institute of Technology School of Materials Science and Engineering, Liu, Michael; Georgia Institute of Technology Lu, Peilin; Georgia Institute of Technology Zhao, Enbo; Georgia Institute of Technology, School of Chemistry and Biochemistry Magasinski, Alexander; Georgia Institute of Technology, School of Materials Science and Engineering Liu, Mengting; Georgia Institute of Technology, School of Materials Science and Engineering; Luo, Shunrui; Georgia Institute of Technology McDaniel, Jesse; Georgia Institute of Technology, Chemistry and Biochemistry Yushin, Gleb; Georgia Institute of Technology

ARTICLE

Received 00th
January 20xx,

Accepted 00th
January 20xx

DOI:
10.1039/x0xx00000x

Nanoconfined Iron (III) Fluoride Cathode in NaDFOB Electrolyte: Towards High-Performance Sodium-Ion Batteries†

Zifei Sun,^a Wenbin Fu,^b Michael. Z. Liu,^b Peilin Lu,^b Enbo Zhao,^a Alexandre Magasinski,^b Mengting Liu,^{bc} Shunrui Luo,^{bd} Jesse McDaniel^a and Gleb Yushin^{*b}

Iron (III) fluoride (FeF₃) is considered as a potential cathode for sodium-ion batteries (SIBs) due to its high capacity and low cost. However, the particle pulverization upon cycling generally results in rapid degradations in its structure and capacity. Here, we introduce a free-standing nanoconfined FeF₃ cathode and a novel electrolyte salt sodium-difluoro(oxalato)borate (NaDFOB) for SIBs. The assembled cells show high discharge capacity up to ~ 230 mAh g⁻¹ at the rate of 20 mA g⁻¹ (~ 200 mAh g⁻¹ at 100 mA g⁻¹) and capacity retention up to ~ 70% after 100 cycles, which represent the best results reported on FeF₃ in Na-ion electrolytes. The achieved high performance can be attributed to the synergic protection provided by the nanoconfined FeF₃ electrode and the NaDFOB electrolyte. Post-mortem analysis and quantum mechanics show that DFOB anion facilitated the formation of a thin cathode electrolyte interphase (CEI) at the surface of FeF₃-carbon nanofibers (CNFs) via oligomerization.

Introduction

Lithium-ion batteries (LIBs) have been of long-held research interest for electrical energy storage due to their energy/power density and long cycle life, but the high price and scarcity of electrode materials may limit their applications, particularly for more cost-sensitive applications, such as mass-market electrical transportation and grid energy storage.^{1,2} As a potential alternative, sodium-ion batteries (SIBs) have attracted great attention due to the much lower cost and larger abundance of sodium compounds.³⁻⁶ Currently, the cathode materials for SIBs are intercalation compounds,

such as metal oxides (e.g. NaMnO₂), polyanionic compounds (e.g. NaFePO₄, Na₃V₂(PO₄)₃), and hexacyanometalates (e.g. Na₂Mn[Mn(CN)₆]), to name a few.⁷⁻¹⁰ However, these materials typically suffer from low specific and volumetric capacities, which could impede their further applications.

Unlike intercalation materials, conversion-type cathodes have the ability to accommodate more than one sodium cation per unit.¹¹⁻¹³ Among them, iron trifluoride (FeF₃) is considered as one of the most attractive candidates due to: (1) the extremely low price of Fe (~ \$0.2 kg⁻¹, which is two orders of magnitude lower than that for cobalt (Co), ~ \$30 kg⁻¹ currently, and nickel (Ni), ~ \$18 kg⁻¹ currently), (2) Fe dramatically better environmental and health friendliness compared to highly toxic Co and toxic Ni, (3) Fe abundance (two and three orders of magnitude larger world reserves of Fe compared to Ni and Co, respectfully), and (4) high

^a School of Chemistry and Biochemistry, Georgia Institute of Technology, Atlanta, GA, 30332, US

^b School of Materials Science and Engineering, Georgia Institute of Technology, Atlanta, GA 30326, USA. E-mail: yushin@gatech.edu

^c School of Physical Science and Technology, Lanzhou University, Lanzhou 730000, China

^d School of Chemistry and Chemical Engineering, Chongqing University, Chongqing 40044, China

^e †Electronic Supplementary Information (ESI) available: See DOI: 10.1039/x0xx00000x

theoretical specific capacity of FeF_3 (712 mAh g^{-1} , over 3 times higher than that of intercalation-type cathodes for SIBs).¹⁴⁻¹⁸ To realize the theoretical value, in principle, FeF_3 is required to undergo a three-electron transfer, which eventually converts it to NaF and metallic Fe .¹⁹ However, such a conversion reaction could also reduce electrode cycle stability. For example, the conversion reaction could lead to a large volume change, which may induce irreversible damages to the electrode structure. In addition, Fe^{3+} may dissolve into electrolyte during the conversion reaction, leading to a “Fe loss”. One solution to address these issues is to construct a protective layer at the surface of the electrodes.²⁰ In the simplest case, the protective surface layer may form in-situ during cycling upon electrolyte reduction.⁶

Electrolytes play an important role in the formation of a stable electrode/electrolyte interphases (often called cathode solid electrolyte interphase (CEI) layer). The salt composition in the electrolytes, in particular, highly influences the CEI composition and cell stability. Likely due to the low cost, NaClO_4 and NaPF_6 were widely used in the previous studies to improve the stability of cell.⁶ For example, Swoyer and coworkers improve the capacity retention of NaVPO_4F by using 1 M NaClO_4 in EC:DEC (2:1) as the electrolyte.²¹ Adelhelm and his coworkers showed that a protective thin film can be induced by using 0.5 M NaPF_6 in EC:DMC and improve the reversibility of $\text{Na}_{0.7}\text{CoO}_2$ -based battery system.²² However, the notorious difficulty in drying NaClO_4 and the potential production of corrosive HF from NaPF_6 limit applications of these two salts.²³

Besides the electrolyte salts, it was reported that electrolyte solvents may similarly have a profound effect on the anode stability in the SIBs and the use of propylene carbonate (PC), for example, allowed much better cycle stability than other solvents, such as dimethyl carbonate (DMC) and 1,2-dimethoxy-ethane (DME), in some cells.²⁴ Electrolyte additives (a minor component of solvent or salt mixture) is another effective approach to improve the cycling stability in SIB cells. For example, the fluoroethylene carbonate (FEC) additive was shown to improve the stability of a tin (Sb) anode for SIBs.²⁵ Despite these promising observations in cells with some selected anode and cathode chemistries, the impact of SIB electrolyte composition

on the performance of FeF_3 cathodes has not been studied in details.

Recently, NaDFOB was found that it has excellent characteristics such as wide electrochemical window and lower viscosity.²⁶ It has been explored in SIBs to achieve an enhanced cycling stability by forming improved solid electrolyte interphase (SEI) on the anode surface.²⁷ The NaDFOB was dissolved in single/binary solvents in these works and used in combination with intercalation cathodes, such as Prussian blue and $\text{Na}_{0.44}\text{MnO}_2$. The effect of ternary solvent system for NaDFOB and its compatibility with conversion-type cathodes, such as FeF_3 , remain unclear.

To address these challenges and gaps in knowledge, here we have developed a FeF_3 -C nanocomposite cathode together with an advanced ternary electrolyte based on sodium-difluoro(oxalato)borate (NaDFOB) for SIBs. In the composite, nanosized FeF_3 confined into carbon nanofiber (NF) matrix to improve structure stability. Electrochemical tests indicate that the FeF_3 SIB cells using NaDFOB in a ternary solvent system can achieve a high capacity for 120 cycles. To get deeper insights on the electrolyte effect, we studied the influence of different salt composition and solvent combination on cell stability. Based on post-mortem analysis and quantum mechanics (QM) calculations, we proposed a possible mechanism for the enhancement of FeF_3 cathode performance in SIB cells via formation of a favorable CEI.

Results and Discussion

In this study, the free-standing FeF_3 -CNF electrodes were produced using an electrospinning-based strategy.¹⁹ As illustrated in Fig. 1a, an electrospun membrane composed of $\text{Fe}(\text{acac})_3$ /polyacrylonitrile (PAN) NFs was carbonized at 600 °C in Ar and reduced at 500 °C in a mixed gas of H_2/Ar to form a Fe-C composite NF. Then, a low-temperature (300 °C) fluorination was conducted to convert the Fe into FeF_3 without sacrificing the carbon matrix. Such a free-standing structure with active FeF_3 embedded in conductive C matrix demonstrates several advantages in structure and electrochemical properties. As demonstrated in Fig. 1b, the C matrix network not only serves as a stable host to protect the FeF_3 from dissolution, but also promotes the electron/ion transport due to its conductive and porous structure. More importantly, the NaDFOB electrolyte will be shown to generate a CEI layer on the electrode surface to prevent the Fe^{3+} losses upon long-term cycling.

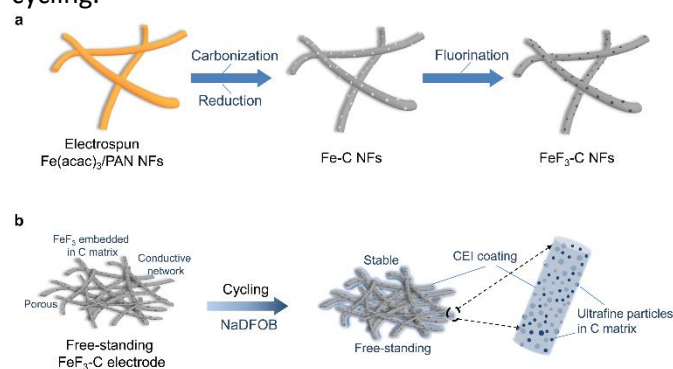


Fig. 1. (a) Schematic illustration of the synthesis of FeF_3 -C nanofibers. (b) The FeF_3 -C electrode cycled in NaDFOB.

Fig. 2a show an X-ray diffraction (XRD) pattern of the obtained product and the typical peaks match well with hexagonal FeF_3 crystal structure (JCPDS #33-0647, space group R3c). Note that the FeF_3 -C structure is free-standing and can be directly used as an electrode without any additive, binder and current collector (Inset of Fig. 2a), which makes it a promise for flexible and light weight energy storage. The scanning electron microscopy (SEM) images (Fig. 2b, c) indicate the FeF_3 -C composite is composed of NFs with FeF_3 nanoparticles embedded into the NFs or on the surface. Such a NF

network generally has a high surface area and good porosity.

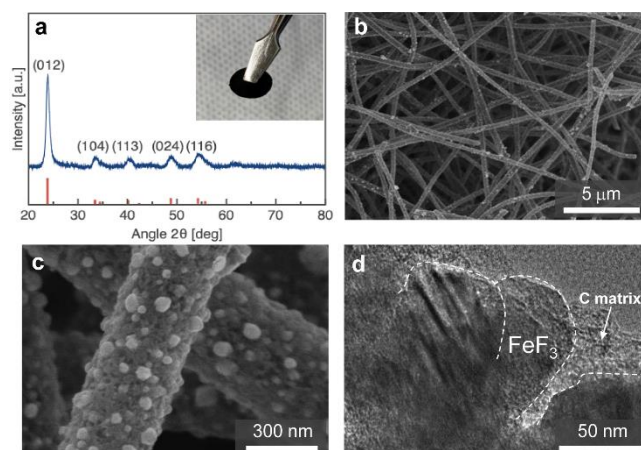


Fig. 2. a) XRD pattern of cathode materials. b) SEM images of FeF_3 /CNFs c) Zoomed in SEM images of FeF_3 /CNFs using carbonization temperature at 600 °C d) high resolution TEM for fluorinated FeF_3 -CNFs.

Transmission electron microscopy (TEM, Fig. 2d) shows that FeF_3 crystals are well confined by carbon matrix which is expected to improve its structure stability. To investigate the electrochemical performance of FeF_3 -CNF composite, we assembled coin-type half cells using the composites as the cathode and a Na metal foil as the counter/reference electrode. To study the impact of Na salts on the cell performance, we selected three Na salts (NaClO_4 , NaPF_6 or NaDFOB) and respectively dissolved them into a mixed solvent of ethylene carbonate (EC), diethylene carbonate (DEC), dimethyl carbonate (DMC) with a volume ratio of 2:1:1 as the electrolytes. The FeF_3 -based cells were first cycled for 120 cycles at a current density of 100 mA g^{-1} in the voltage window of 1.2–4.2 V. As shown in Fig. 3a, we find the cells using NaDFOB exhibit the most stable performance during the first 120 cycles. At the 50th cycle, the hysteresis of the cells using NaDFOB drops the least compared with those using NaPF_6 and NaClO_4 (Fig. 3b). When compare the capacity drop from 3rd cycle to 50th cycle, the FeF_3 cells based on NaDFOB drop 21.7% (Fig. S1a[†]), which is much better than the cells with NaPF_6 (51.5%, Fig. S1b[†]) and NaClO_4 (47.7%, Fig. S1c[†]).

To explore the effect of electrolyte solvents on the cycling performance of Na- FeF_3 cells, we selected three mixed solvents for comparison, including EC:DEC:DMC (2:1:1 in volume), EC:DEC (1:1 in volume) and EC:DMC

(1:1 in volume). As clearly shown in Fig. 3c, the cells based on EC:DEC:DMC exhibit the best performance among them. After 120 cycles, their capacity retains up to 69.4%, much better than the cells comprising EC:DEC (28.17%) and EC:DMC (31.4%) solvent mixtures. Moreover, we find that the cell with EC:DEC:DMC solvent mixture shows a much smaller voltage hysteresis compared to others, which means the ternary mixed solvent has the potential to increase the energy efficiency and enhance the conversion kinetics of FeF_3 cathodes. Besides, we compared the voltage profiles at 10th and 50th cycles of the cells using different electrolytes (Fig. S2[†]). The cell with ternary solvents does not show any visible hysteresis change between 10th to 50th cycle, while the cells with binary solvent systems (EC:DMC and EC:DEC) suffer from a sharp increase in their voltage hysteresis, which indicates the ternary solvent system is more stable for the NaDFOB electrolyte in FeF_3 SIBs.

In addition to visible electrolyte dependence, the cut-off cell voltage is also important for maintaining stable performance and high capacity in FeF_3 cathodes. If we compare the cells with 1M NaDFOB and 1M NaClO_4 electrolytes (in EC:DEC:DMC) cycled within different voltage ranges (1.2–4.2 V and 1.5–3.7 V) we find that 1.2–4.2 V works better for the cells containing 1M NaClO_4 or 1M NaDFOB (Fig. S3[†]). The possible reason could be the following: first, wider voltage range should increase driving force for Na ion diffusion and thus enable higher accessible capacity. Second, broader voltage range may induce more favorable CEI stability. Indeed, the conversion peak gradually decreases for the samples cycling under 1.5–3.7 V (Fig. S4[†]) but remains much more stable for samples cycling within 1.2–4.2 V (Fig. 4c). Considering the conversion capacity contributes to 2/3 of the total capacity (712 mAh g^{-1}), it's not surprising to find that the attainable capacity is better in 1.2–4.2 V than 1.5–3.7 V. It is worth to notice that the performance of 1M NaDFOB in EC:DEC:DMC is still better than 1M NaClO_4 in EC:DEC:DMC under these two different voltage ranges even though both of them perform the best in the 1.2–4.2 V voltage window (Fig. 4a and Fig. 4b). The coulombic efficiency (CE) of NaClO_4 is larger than 100% at the first 12 cycles under the voltage range of 1.2–4.2 V and keeps a constantly larger CE value (>100%) with

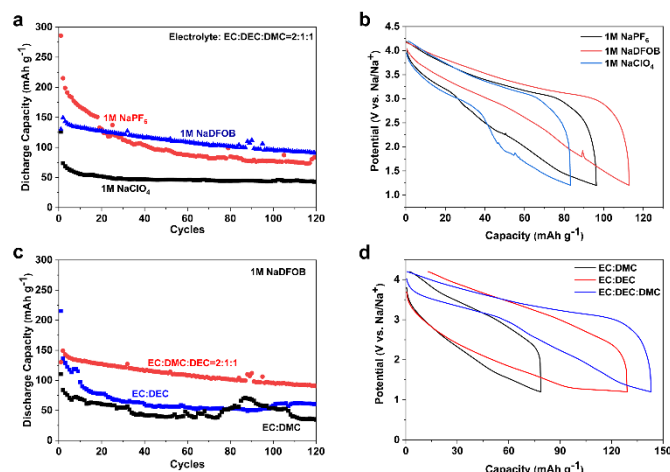


Fig. 3. a) Capacity comparison under 1.2–4.2 V between different salt at the concentration of 1M in EC:DEC:DMC. b) Capacity comparison under 1.2–4.2 V in EC:DEC:DMC=2:1:1 using different electrolyte salt at 50th cycle. c) Capacity comparison under 1.2–4.2 V of 1M NaDFOB dissolved in different solvents. d) 3rd cycle capacity comparison between different solvents.

an average at 102% under the voltage range of 1.5–3.7 V. Higher than 100% CE indicates the presence of side reactions between electrolyte and electrode. Compared with NaClO_4 , the use of NaDFOB electrolyte results in the CE reducing to below 100% from the 4th cycle and has an average value of $\sim 100\%$ under the voltage range of 1.5–3.7 V (Fig. 4a and 4b). Formation of the CEI during the first three cycles in NaDFOB is responsible for its high CE. After the CEI forms, this thin protective film prevents the further reaction between FeF_3 and electrolyte. Compared with NaDFOB cell, NaClO_4 cell exhibits continuous side reactions taking place between FeF_3 and electrolyte for more than 3 cycles. This side reaction generates thicker CEI covering the surface of the electrode and likely limiting the Na diffusion through the CEI. NaClO_4 cell has an even thicker CEI under the voltage range of 1.5–3.7 V which has been indicated by the constantly larger value of CE (>100%). As a result, the capacity of 1.5–3.7 V decreases compared with 1.2–4.2 V.

Based on our cyclic voltammetry (CV) studies, the FeF_3 -C cells exhibit typical redox peaks in both charge and discharge regions (Fig. 4c). In the discharge portion, the first peak at ~ 3.3 V (vs Na/Na^+) gradually increases in intensity as cycle number increases and splits into two separate peaks closely positioned at ~ 3.25 and 3.4 V vs Na/Na^+ by the 6th cycle. In contrast, the peak observed

at a lower potential of ~ 2.4 V vs. Na/Na⁺ decreases in intensity dramatically throughout the initial cycling process. These two phenomena suggest that the electrochemical activity of the high-potential reaction occurring at ~ 3.4 V increases, while the process occurring at the lower potential exhibits poor reversibility and gradually reduces its contribution to capacity. Based on the peak location and polarization (difference in the position of the corresponding oxidation and reduction peaks), the first peak can correspond to the intercalation of Na⁺ into the FeF₃ while the second peak likely corresponds to the conversion reaction.²⁸ Indeed, the difference in oxidation and reduction potentials is quickly becoming very small (<0.1 V) for the 1st peak, which is typical for intercalation reactions. Interestingly, the 1st peak position (3.4 V vs Na/Na⁺) is slightly above the theoretical value (3.1 V) when Na intercalates into FeF₃ to form Na_xFeF₃ according to our calculations conducted using previously reported Gibbs free energies.²⁹ We speculate that the small difference may be related to inaccuracies in the free energy estimations or possibly to changes in the nano-sized electrode chemistry (e.g., oxygenation) during cycling. Due to large size of Na⁺ (116 pm vs. 90 pm for Li⁺) its insertion into FeF₃ nanoparticles is expected to induce significant strain and the additional strain energy storage may affect the cell voltage.³⁰ We also speculate that the observed splitting the higher voltage peaks may be related to the incorporation of oxygen into the FeF₃ surface structure and the lower potential may be expected for the partially oxygenated portion of the material (FeO_xF_{3-2x}).³¹ It is found that a small tail at the end of discharge cycles (~ 1.0 V) is gradually disappearing as the cycle increases, which could be associated with the electrolyte reduction and CEI passivation.³²

We then cycled the FeF₃-C cathodes in 1 M NaDFOB (EC:DEC:DMC) using different current densities (such as 100 and 20 mA g⁻¹ in Fig. 4d, for example). At a low current density (20 mA g⁻¹), the cells show much higher discharge capacities (over 220 mAh g⁻¹) at first few cycles but undergo a faster capacity degradation compared to those using a higher rate (100 mA g⁻¹). We hypothesize that the significantly slower conversion reaction is more pronounced at smaller currents and its low reversibility triggers faster cell fading. Fig. 4c shows the charge-

discharge polarization curves clearly highlighting the evolution of the electrochemical reactions and significant differences in the voltage hysteresis corresponding to these two Na insertion/extraction mechanisms. Initial very high overpotential for Na⁺ insertion into FeF₃ is similar to that observed in earlier studies for Li⁺ insertion and may be related to (i) volume changes, (ii) slow electrolyte intercalation into the FeF₃/CNF and (iii) plastic deformation and the formation of new surfaces and interfaces (Fe/C, NaF/F, Fe/CEI, NaF/CEI, C/CEI, etc.).¹⁹ By cycle 3 intercalation reaction capacity is ~ 120 mAh g⁻¹ ($\sim 50\%$ of 237 mAh g⁻¹ theoretical value) and conversion reaction capacity is ~ 110 mAh g⁻¹ ($\sim 23\%$ of 475 mAh g⁻¹ theoretical value) for the total combined capacity of ~ 230 mAh g⁻¹. The incompleteness of the intercalation reaction was somewhat surprising and may be explained by (i) relatively large size of insulative FeF₃ domains, (ii) growing strain energy barrier at higher capacities or (iii) the 1st cycle partial conversion reaction destroying or insulating some of the FeF₃ nanoparticles.³³ The incompleteness of the conversion reaction may similarly be explained by the first two factors and also by (iv) the compressive stresses imposed on active material by carbon matrix as active material attempts to expand by nearly 2x in volume.³⁴ The intercalation capacity remains rather stable for the first 10 cycles, while the conversion reaction capacity fades, reducing the combined capacity to below 210 mAh g⁻¹ at cycle 10. However, subsequent cycling to 100th cycle could destroy the intercalation plateau as well, as evidenced by the dramatic increase in the voltage hysteresis. We propose that the visible lack of the reversibility of the conversion reaction destroys crystalline FeF₃ domains, leaving unreacted NaF, Fe and possibly CEI in between (since carbon in CNF is porous electrolyte may still reach active material and decompose upon a direct contact with Fe nanoparticles due to their catalytic effect).³⁵ Fig. S5† and Fig. 4e show the hysteresis and capacity drop of NaDFOB and NaClO₄ at 2nd, 3rd and 50th cycle. Clearly, NaDFOB has better cycling stability over NaClO₄ and the capacity drops from 149.26 mAh g⁻¹ at 2nd cycle to 112.92 mAh g⁻¹ at 50th cycle, which is 75.6% capacity retention. Compared with NaDFOB, NaClO₄ exhibits much lower capacity retention and its capacity drops from 233.36 mAh g⁻¹ at 2nd cycle to 88.99 mAh g⁻¹ at 50th cycle which is 38.13% capacity

retention. As compared in Fig. 4f, the cycling performance of our free-standing $\text{FeF}_3\text{-C}$ cathodes ($\sim 100 \text{ mAh g}^{-1}$ after 120 cycles) is noticeably superior compared to spherical $\text{FeF}_3\cdot 0.33\text{H}_2\text{O}/\text{MWCNTs}$ ($\sim 75 \text{ mAh g}^{-1}$ after 100 cycles), $\text{FeF}_3/\text{graphene}$ composite ($\sim 96 \text{ mAh g}^{-1}$ after 30 cycles), $\text{FeF}_3\cdot 0.5\text{H}_2\text{O}$ ($\sim 70 \text{ mAh g}^{-1}$ after 50 cycles) and NaFeF_3 ($\sim 86 \text{ mAh}$

electrolyte. At 700°C , noticeable size ripening is found and therefore could decrease the size effects.^{40, 41} Besides, temperature influences the size of FeF_3 domains. FeF_3 domains tend to coarsen once the temperature increase. Third, the weight percentage of FeF_3 increases from 36 to 56 and 60 wt.% with increasing annealing temperature from 500°C to 600°C and 700°C .

Long-term testing and rate performance were also tested. As shown in Fig. S8†, discharge capacity is $\sim 150 \text{ mAh g}^{-1}$ at 2nd cycle and slowly drops to $\sim 58\%$ of the initial capacity at the 200th cycle. At the small current density of 25 mA g^{-1} the discharge capacity is rather high (205 mAh g^{-1}). It reduced to 163 mAh g^{-1} at 50 mA g^{-1} , 128 mAh g^{-1} at 75 mA g^{-1} and 108 mAh g^{-1} at 100 mA g^{-1} (Fig. S9†).

Post-mortem analysis provides further insights into the reaction and degradation mechanisms of $\text{FeF}_3\text{-C}$ cathode cycled in NaDFOB electrolyte. After 120 cycles, the cells were disassembled and the cycled $\text{FeF}_3\text{-C}$ electrodes were characterized using SEM, TEM and X-ray photoelectron spectroscopy (XPS). Compared images before (Fig. 5a) and after cycling (Fig. 5b-d), we observed a thin CEI film generated at the surface of cathode during cycling. The thickness of CEI was collected from multiple places and calculated the average thickness of CEI is $\sim 1.6 \text{ nm}$. We further explored the components inside of CEI by using a high resolution XPS. Compared with the XPS survey spectrum before charging/discharging (Fig. S10†), we found B-O and B-F bonds after 120 cycles (Fig. 5e).

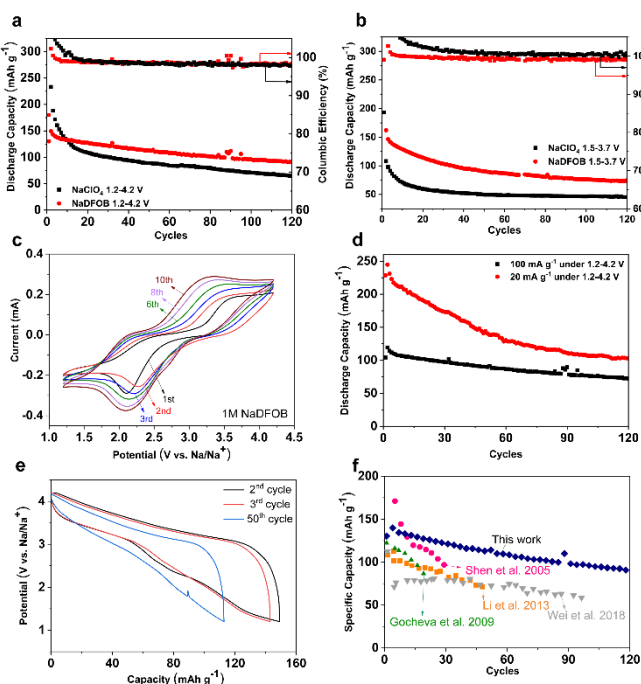


Fig. 4. a) Capacity comparison between 1M NaClO_4 and 1M NaDFOB in EC:DEC:DMC under 1.2-4.2 V. b) Capacity comparison between 1M NaClO_4 and 1M NaDFOB in EC:DEC:DMC under 1.2-4.2 V. c) CV diagram for 1M NaDFOB under the voltage range of 1.2-4.2 V. d) 1M NaDFOB rate capacity comparison under 1.2-4.2 V. e) Charge/discharge curve for cells under 1.2-4.2v at 2nd, 3rd and 50th cycle using 1M NaDFOB. f) Capacity comparison between this work and other group's work.

g^{-1} after 20 cycles) as cathode materials.³⁶⁻³⁹ In addition, we compared the $\text{FeF}_3\text{-C}$ samples using different carbonization temperatures (from 500 to 700°C) in the synthesis process. These samples show a similar nanofiber morphology (Fig. S6†). However, as shown in Fig. S7†, the sample after 600°C still exhibits the best performance (1.2–4.2 V) during 120 cycles among them. This could be attributed to following reasons. First, 600°C sample had higher percentage of FeF_3 exposed at the surface compared with 500°C sample, which can increase the contact between active FeF_3 with

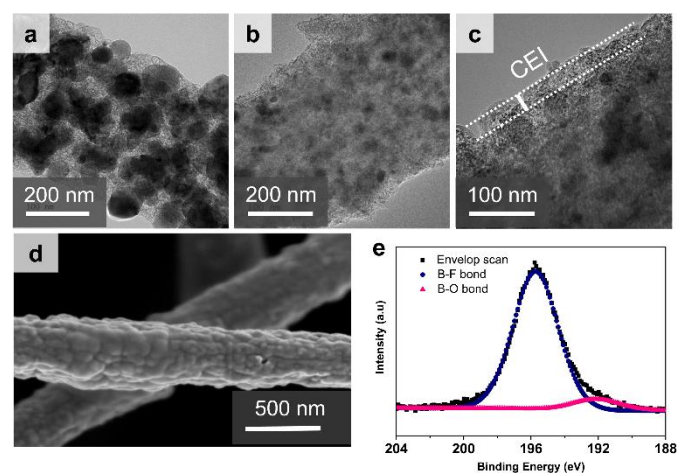


Fig. 5. a) scanning electron microscopy of cathode materials before 120 cycles b,c) TEM images of NFs

after charging/discharging for 120 cycles, d) SEM image for cathode materials after cycling. e) high resolution x-ray photoelectron spectroscopy of the B_{1s} scan in the cycled NF.

To get additional insights into the electrolyte decomposition and the CEI formation during cycling, we performed quantum mechanical (QM) calculations based on previously discussed experimental observations. We restricted our QM as follows: 1) only reductive electrolyte decomposition pathways were investigated, consistent with discussion of the experimental CV data; 2) any decomposition mechanisms leading to formation of CO and/or CO₂ were not considered, as there was no observed gas formation during experimental cycling;⁴² 3) since XPS peaks indicate either B-F and/or B-O bonds within the CEI layer, QM calculations focused on products consistent with these features. We predict an energetically accessible pathway for reduction-mediated, radical oligomerization/polymerization of DFOB anions (in surrounding ionic media) and suggest that such DFOB oligomers/polymers could be an important component of CEI films. Our computed pathway for DFOB dimerization is schematically depicted in Fig. 6, and further oligomerization would proceed through analogous steps (without additional reduction), until the radical is quenched (either by a side reaction and/or subsequent oxidation/reduction). For all species involved in the dimerization pathway, the electron density of the radical electron was computed and is shown as solid blue isosurface in Fig. 6. Initially, we consider a single DFOB anion that is coordinated by two sodium ions [Na₂-DFOB]⁺, with sodium coordination being energetically favorable and also facilitating reduction.⁴² In the optimized structure, Na⁺ ions are ~ 2.15–2.2 Å coordination distances from oxygen and fluorine atoms of the anion. We predict a reduction potential of ~ 2 V relative to Na/Na⁺ for [Na₂-DFOB]⁺ species, which approximately matches the reduction peaks in the experimental CV curve. Note that several tenths of eV uncertainty/error is expected for these calculations when comparing to experiment, due to lack of solvent in calculations, and neglect of solvent shifts in absolute Na/Na⁺ redox potential when extrapolating calculated to reference values.³²

The reduction of [Na₂-DFOB]⁺ to the [Na₂-DFOB][•] radical results in localization of the radical electron density primarily within orbitals of the oxalate moiety, as shown in the solid blue isosurface (Step 1, Fig. 6). However, we find an energetically favorable Na⁺-mediated ring-opening rearrangement that results in transfer of the radical electron density to the boron atom of the –BF₂ group, which precedes dimerization. Ring opening is largely driven by favorable ionic interactions formed between Na⁺ and the oxygen and –BF₂ group on alternate ends of the ring-opened anion. The transition state for the [Na₂-DFOB][•] ring opening step (Step 2, Fig. 6) is most likely solvent/ion mediated, with free energy barriers dependent on electrolyte composition/ion concentration—however, for our cluster model, the net process is energetically downhill (favorable), with ΔE = –26 kcal/mol. After ring-opening, the [Na₂-DFOB][•] species can dimerize by boron-radical attack of an oxalate group on another nearby DFOB anion. Note that this transfer of radical to the second DFOB oxalate group (Step 3, Fig. 6) results in a very similar radical electron density as in the initial DFOB reduction, localized on the oxalate (Step 1). While dimerization of DFOB requires close spatial proximity of anions, this is energetically enabled by the coordinating Na⁺ ions in the electrolyte; we predict that such [Na₂-DFOB]²⁺ dimers are bound by several to tens of kcal/mol relative to isolated Na₂-DFOB species. As shown in Step 3, Fig. 6, dimerization proceeds by radical attack (boron atom) on the second DFOB anion at the oxygen ring atom; the second DFOB can then ring open as before, transferring the radical electron density to the opposing boron atom (Step 4). This radical-polymerization can continue (until radical quenching) to form larger DFOB oligomers and/or polymers, which are expected to be incorporated into the CEI as moderately-sized oligomers are most likely insoluble within the electrolyte. While the last ring opening step (Step 4) is predicted to be somewhat energetically unfavorable (ΔE = 15 kcal/mol) in our cluster model calculations, this step is solvent/ion mediated, and free energy barriers will depend on solvent/ion concentration. Additionally, incorporation of moderately sized oligomers into the CEI will lead to irreversibility of the backwards reaction and shift the equilibrium towards further oligomerization.

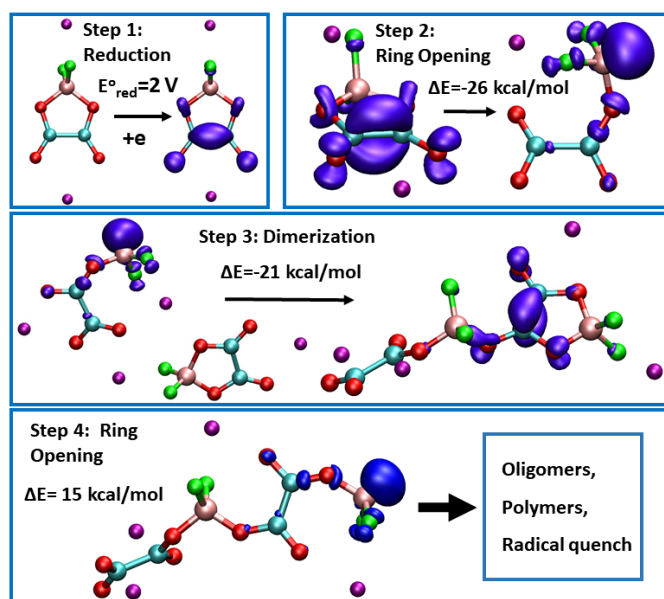


Fig. 6. Schematic of reduction-mediated, DFOB oligomerization pathway. In step 1, DFOB coordinated by two Na cations is reduced to form a radical; the radical spontaneously ring opens in step 2, with the radical electron density transferred to the boron atom. In step 3, the radical species attacks another DFOB anion (coordinated by two Na) and forms a dimer through a new B-O bond, ring opening the second DFOB in step 4. This mechanism can continue to form larger oligomers, until the radical is quenched. Color scheme is: carbon, cyan; oxygen, red; boron, pink; fluorine, green; sodium ions, purple. Solid blue denotes 0.01 electron density isosurface of excess radical electron.

Conclusion

In summary, we have successfully developed cells based on a high-capacity nanoconfined FeF_3 SIB cathode produced by an electrospinning of PAN- $\text{Fe}(\text{acac})_3$ solution followed by carbonization and fluorination. The FeF_3 nanoparticles in such composites are imbedded into a flexible and porous carbon nanofiber matrix to provide electronically conductive media for electron transport, minimize agglomeration of active material and mitigate volume changes during charging and discharging. Carbonization temperature of ~ 600 °C was found to be the most optimal for attaining the best electrochemical performance – substantially lower

temperature was insufficient for archiving high electrical conductivity, while substantially higher temperature resulted in excessive coarsening of active nanoparticles. Performance of different electrolyte salts (NaClO_4 , NaDFOB , NaPF_6) and different mixtures of organic solvent (EC:DEC, EC:DMC, EC:DEC:DMC) were compared. The use of NaDFOB salt in the ternary electrolyte (EC:DEC:DMC) was found reach the best cycling performance and enabled the development of a thin and conformal protective CEI film on cathode, which resulted in greatly improved cycling performance compared to traditionally used $\text{NaClO}_4/\text{NaPF}_6$. Quantum chemistry calculations suggested that polymerization of the NaDFOB may likely be responsible for the formation of this favorable CEI.

Experimental Section

Synthesis of FeF_3 -CNFs cathode materials

First, 1g PAN ($M_w=150000$, sigma-Aldrich) was dissolved into 11.5 g N,N-dimethylformamide (Sigma-Aldrich, USA) by stirring overnight at 65 °C. Then 1.5 g ferric acetylacetonate ($\text{Fe}(\text{acac})_3$, Alfa Aesar, USA) was added to the solution and stirred overnight to obtain homogenous solution. 3 ml of the obtained solution was loaded into a syringe with a clipped needle. Electrospinning was carried out under 20 kV for 3 h and used an aluminum (Al) foil as the collector. The distance between the tip of the needle and Al foil was 20 cm. After electrospinning, the precursor membrane was peeled off from the Al foil and was first stabilized in air at 220 °C for 1 hour and was carbonized in Ar at either 500, 600, or 700 °C for 2 hours from a ramp rate of 2 °C /min. The product was subsequently reduced in H_2 (4% hydrogen in Argon, Airgas) at 500 °C for 1 hour and fluorinated in NF_3 gas (2% NF_3 in helium, Linde Electronics & Specialty Gases, USA) at 300 °C for 2 hours to produce FeF_3 -CNFs. After synthesis, the materials were stored in an inert environment to prevent degradation.

Materials Characterization

XRD patterns were collected on a X'Pert PRO Alpha-1 (PANalytical, The Netherlands) with a Cu K α radiation at 400 kV, XPS was carried out K-Alpha system (Thermo Scientific, USA). SEM images, and SEM conducted by Hitachi SU8010 (Japan) and Zeiss Ultra 60 respectively. TEM images were collected using a Tecnai G2 F30, (FEI, The Netherlands). TGA was performed on a Q600 TGA/DSC system (TA Instruments, USA).

Electrochemical Characterization

The as-prepared FeF₃-CNFs were used without any additional current collectors as electrodes to make 2032 type coin cells. Sodium metal acted as the counter and reference electrode, and a glass fiber membrane (Whatman) was used as the separator. The electrolyte salt-NaDFOB was synthesized through the reaction of sodium oxalate and BF₃·ether. ⁴³ 1M NaDFOB, 1M NaPF₆ and 1M NaClO₄ was dissolved into ethylene carbonate: dimethyl carbonate (Sigma-Aldrich, EC: DEC: DMC=2:1:1 in volume) as the electrolyte. All cells were assembled in Ar-filled glove box. Cyclic voltammetry (CV) and EIS were conducted using Gamry Reference 600 potentiostat (Gamry Instruments, Inc., USA). Galvanostatic charge-discharge tests were performed on an Arbin instrument (Arbin BT-2043).

Calculation Details

All capacity used in this paper was calculated based on the active materials (FeF₃) weight percentage.

All quantum mechanical calculations were conducted with the Psi4 software package, employing an aug-cc-pvdz basis set.⁴⁴ Geometries and energies were computed at the MP2 level of theory, employing density-fitting and a frozen-core approximation, and UHF reference wavefunctions were used for the radical species. MP2 was chosen instead of alternative DFT methods based on preliminary calculations in which PBE0 and B3LYP gave a poor description of the reduced DFOB radical, with electron density spilling over to nearby sodium ions and related SCF convergence problems.

Conflicts of Interest

The authors declare no conflict of interest.

Acknowledgements

This work was largely supported by ARO (Grant No. W911NF-17-1-0053). Wenbin Fu, Mengting Liu and Shunrui Luo acknowledge the fellowship support of China Scholarship Council.

Notes and references

1. N. Nitta, F. Wu, J. T. Lee and G. Yushin, *Materials Today*, 2015, **18**, 252-264.
2. B. Scrosati and J. Garche, *Journal of Power Sources*, 2010, **195**, 2419-2430.
3. S.-W. Kim, D.-H. Seo, X. Ma, G. Ceder and K. Kang, *Advanced Energy Materials*, 2012, **2**, 710-721.
4. M. D. Slater, D. Kim, E. Lee and C. S. Johnson, *Advanced Functional Materials*, 2013, **23**, 947-958.
5. C. Vaalma, D. Buchholz, M. Weil and S. Passerini, *Nature Reviews Materials*, 2018, **3**, 18013.
6. A. Ponrouch, D. Monti, A. Boschini, B. Steen, P. Johansson and M. R. Palacín, *Journal of Materials Chemistry A*, 2015, **3**, 22-42.
7. J. Billaud, R. J. Clément, A. R. Armstrong, J. Canales-Vázquez, P. Rozier, C. P. Grey and P. G. Bruce, *Journal of the American Chemical Society*, 2014, **136**, 17243-17248.
8. J. Kim, D.-H. Seo, H. Kim, I. Park, J.-K. Yoo, S.-K. Jung, Y.-U. Park, W. A. Goddard III and K. Kang, *Energy & Environmental Science*, 2015, **8**, 540-545.
9. Z. Jian, W. Han, X. Lu, H. Yang, Y.-S. Hu, J. Zhou, Z. Zhou, J. Li, W. Chen, D. Chen and L. Chen, *Advanced Energy Materials*, 2013, **3**, 156-160.
10. H.-W. Lee, R. Y. Wang, M. Pasta, S. Woo Lee, N. Liu and Y. Cui, *Nature Communications*, 2014, **5**, 5280.
11. F. Wu and G. Yushin, *Energy & Environmental Science*, 2017, **10**, 435-459.
12. Y. Fang, B. Y. Guan, D. Luan and X. W. Lou, *Angewandte Chemie*, 2019, **131**, 7821-7825.
13. T. Zhu, P. Hu, X. Wang, Z. Liu, W. Luo, K. A. Owusu, W. Cao, C. Shi, J. Li, L. Zhou and L. Mai, *Advanced Energy Materials*, 2019, **9**, 1803436.

14. F. Wu, O. Borodin and G. Yushin, *MRS Energy & Sustainability*, 2017, **4**, E9.
15. J. M. D. Coey, *Scripta Materialia*, 2012, **67**, 524-529.
16. O. Dary, *Nutrition Reviews*, 2002, **60**, S34-S41.
17. J. R. Hernández-Tapia, J. Vazquez-Arenas and I. González, *Journal of Hazardous Materials*, 2013, **262**, 709-716.
18. Y. Lu, Z.-y. Wen, J. Jin, X.-w. Wu and K. Rui, *Chemical Communications*, 2014, **50**, 6487-6490.
19. W. Fu, E. Zhao, Z. Sun, X. Ren, A. Magasinski and G. Yushin, *Advanced Functional Materials*, 2018, **28**, 1801711.
20. Z. Chen, L. Xu, Q. Chen, P. Hu, Z. Liu, Q. Yu, T. Zhu, H. Liu, G. Hu, Z. Zhu, L. Zhou and L. Mai, *Journal of Materials Chemistry A*, 2019, **7**, 6740-6746.
21. J. Barker, M. Y. Saidi and J. L. Swoyer, *Electrochemical and Solid-State Letters*, 2003, **6**, A1-A4.
22. A. Bhide, J. Hofmann, A. Katharina Dürr, J. Janek and P. Adelhelm, *Physical Chemistry Chemical Physics*, 2014, **16**, 1987-1998.
23. D. J. Devlin and P. J. Herley, *Reactivity of Solids*, 1987, **3**, 75-84.
24. A. Ponrouch, E. Marchante, M. Courty, J.-M. Tarascon and M. R. Palacín, *Energy & Environmental Science*, 2012, **5**, 8572-8583.
25. M. K. Sadan, S.-H. Choi, H. H. Kim, C. Kim, G.-B. Cho, K.-W. Kim, N. S. Reddy, J.-H. Ahn and H.-J. Ahn, *Ionics*, 2018, **24**, 753-761.
26. J. Chen, Z. Huang, C. Wang, S. Porter, B. Wang, W. Lie and H. K. Liu, *Chemical Communications*, 2015, **51**, 9809-9812.
27. L. Gao, J. Chen, Y. Liu, Y. Yamauchi, Z. Huang and X. Kong, *Journal of Materials Chemistry A*, 2018, **6**, 12012-12017.
28. P. Liu, J. J. Vajo, J. S. Wang, W. Li and J. Liu, *The Journal of Physical Chemistry C*, 2012, **116**, 6467-6473.
29. C. E. Bamberger, B. F. Hitch and C. F. Baes, *Journal of Inorganic and Nuclear Chemistry*, 1974, **36**, 543-545.
30. X. H. Liu, F. Fan, H. Yang, S. Zhang, J. Y. Huang and T. Zhu, *ACS Nano*, 2013, **7**, 1495-1503.
31. X. Fan, C. Luo, J. Lamb, Y. Zhu, K. Xu and C. Wang, *Nano Letters*, 2015, **15**, 7650-7656.
32. W. Gu, O. Borodin, B. Zdyrko, H.-T. Lin, H. Kim, N. Nitta, J. Huang, A. Magasinski, Z. Milicev, G. Berdichevsky and G. Yushin, *Advanced Functional Materials*, 2016, **26**, 1507-1516.
33. R. Malik, F. Zhou and G. Ceder, *Nature Materials*, 2011, **10**, 587-590.
34. M. T. McDowell, S. Xia and T. Zhu, *Extreme Mechanics Letters*, 2016, **9**, 480-494.
35. J.-L. Shui, N. K. Karan, M. Balasubramanian, S.-Y. Li and D.-J. Liu, *Journal of the American Chemical Society*, 2012, **134**, 16654-16661.
36. S. Wei, X. Wang, M. Liu, R. Zhang, G. Wang and H. Hu, *Journal of Energy Chemistry*, 2018, **27**, 573-581.
37. Y. Shen, X. Wang, H. Hu, M. Jiang, Y. Bai, X. Yang and H. Shu, *RSC Advances*, 2015, **5**, 38277-38282.
38. C. Li, C. Yin, L. Gu, R. E. Dinnebier, X. Mu, P. A. van Aken and J. Maier, *Journal of the American Chemical Society*, 2013, **135**, 11425-11428.
39. I. D. Gocheva, M. Nishijima, T. Doi, S. Okada, J.-i. Yamaki and T. Nishida, *Journal of Power Sources*, 2009, **187**, 247-252.
40. L. Li, F. Meng and S. Jin, *Nano Letters*, 2012, **12**, 6030-6037.
41. Y. Fang, X.-Y. Yu and X. W. Lou, *Matter*, 2019, **1**, 90-114.
42. M. Xu, L. Zhou, L. Hao, L. Xing, W. Li and B. L. Lucht, *Journal of Power Sources*, 2011, **196**, 6794-6801.
43. J. L. Allen, D. W. McOwen, S. A. Delp, E. T. Fox, J. S. Dickmann, S.-D. Han, Z.-B. Zhou, T. R. Jow and W. A. Henderson, *Journal of Power Sources*, 2013, **237**, 104-111.
44. R. M. Parrish, L. A. Burns, D. G. A. Smith, A. C. Simmonett, A. E. DePrince, E. G. Hohenstein, U. Bozkaya, A. Y. Sokolov, R. Di Remigio, R. M. Richard, J. F. Gonthier, A. M. James, H. R. McAlexander, A. Kumar, M. Saitow, X. Wang, B. P. Pritchard, P. Verma, H. F. Schaefer, K. Patkowski, R. A. King, E. F. Valeev, F. A. Evangelista, J. M. Turney, T. D. Crawford and C. D. Sherrill, *Journal of Chemical Theory and Computation*, 2017, **13**, 3185-3197.